Simulating 2D viscous flow around geometries with vertices through the Diffused Vortex Hydrodynamics method

E. Rossi [a,c], A. Colagrossi [a,*], D. Durante [a], G. Graziani [b]

[a] **CNR-INSEAN**, *Marine Technology Research Institute, Rome, Italy.*

[b] **DIMA**, *Department of Mechanical and Aerospace Engineering, Sapienza University of Rome.*

[c] **LHEEA Lab. (ECN / CNRS)**, *École Centrale Nantes, Nantes, France.*

Abstract

The Diffused Vortex Hydrodynamics (DVH) is a recent numerical model born as an evolution of the classical vortex particle methods, where an improvement of the solution quality has been achieved through a regularization of the particles spatial distribution during the vorticity diffusion process. The DVH method is a pure meshless method which adopts a body-fitted approach to enforce no-slip boundary condition on solid surfaces. In the present work it is exploited to perform an accurate analysis of the vorticity field generated by the incompressible flow around bodies with geometrical singularities. In common academic or technological applications, such singularities are quite frequent (*e.g.* trailing edges of wing profiles or of propeller blades) and the classical Euler mesh-based methods can suffer in modelling these geometries. In the recent years a wide literature was produced in order to describe enhanced numerical methods that could overcome such challenging problems. The potentialities of the DVH approach to problems where bodies with geometric singularities are involved, are deeply discussed and some examples are finally offered.

Key words: Vorticity Dynamics, Vortex Method, Particle Methods, Meshless Methods, Diffused Vortex Hydrodynamics, flow around geometrical singularities

* Corresponding author: *Tel.: +39 06 50 299 343; Fax: +39 06 50 70 619.*
Email address: andrea.colagrossi@cnr.it (A. Colagrossi).

1 Introduction

In the last decades, the accurate analysis of the vorticity field generated by a body in motion played an important role in technology applications: aircraft design, helicopter, bridges or skyscrapers are clear examples. Moreover, it proved to be fundamental and strategic for new renewable energy devices. The research on wind turbines farms, in fact, covers a large literature on this topic and a new and interesting challenge is represented by the bladeless evolution of them which exploits the tower oscillations induced by the shed vorticity (see e.g. Villareal [22]).

The numerical simulation of the vorticity field generated by complex bodies represents a non trivial task even at the present days: the algorithms based on the solution of the Navier-Stokes equations in terms of fields (e.g. Finite Differences, Finite Volumes of Finite Elements) or particles (e.g. Smooth Particle Hydrodynamics) are not directly affected by the vorticity calculation as a primary variable, but its evaluation is usually performed in the post processing with an unavoidable accuracy degradation. Moreover, the classical approaches to the description of the flow field around a body generally suffer when geometric singularities are involved, as it may be typical in the naval hydrodynamic environment. The presence of bodies with sharp surfaces frequently forces to exploiting unstructured meshes, that are simpler to generate but less accurate in the convergence control with respect to the structured ones. However, the latter requires a certain regularity of the domains mapped, so a wide literature on numerical techniques, developed in order to overcome these issues, has been produced in the last decades (see for general description of overlapping grids technique Petersson [18] or for naval applications Muscari [15]). In the paper of Marrone *et al.* [11] the δ-SPH approach is addressed in order to study violent water impacts. There, the flow past a sharp-edged obstacle shows a particular effort in dealing with the geometric singularity. To tackle this problem, a ghost-fluid approach was formulated in order to ensure the enforcement of the correct boundary conditions.

Differently from the outlined approaches, the vortex particle methods allow to study the vorticity evolution in a proper way, being the vorticity the primary variable of the problem. In the present paper the Diffused Vortex Hydrodynamics (DVH), presented in Rossi *et al.* [19],[20] is exploited for the modelling of 2D incompressible viscous flow around bodies with geometrical singularities. The DVH method has been validated in Rossi *et al.* [19] where the evolution of vorticity distribution in free space is considered. In Rossi *et al.* [20] the flow at moderate and high Reynolds numbers past smooth bluff bodies of various shapes has been studied and the results were compared with those present in the literature.

The use of a vortex method for incompressible flows brings several advantages (see e.g. Cottet and Koumoutsakos [6], Koumoutsakos and Leonard [9], Chorin [2]):

(i) the pressure field is no longer a direct unknown of the problem when the Navier-Stokes equations are written in vorticity formalism,
(ii) the continuity equation is automatically satisfied,
(iii) the vorticity formulation allows to discretize only the rotational region of the flow (self-adaptivity),
(iv) high accuracy on the evaluation of the velocity field (because it is obtained through a spatial integration),
(v) possibility to simulate flows at high Reynolds numbers,
(vi) the boundary conditions at infinity are automatically satisfied, therefore large spatial domains are not required to correctly enforce them,
(vii) finally, advantage comes from the Lagrangian nature of the method that reduces the numerical dissipation present in mesh-based approach coming from the nonlinear term of the Navier-Stokes equations (see e.g. Cottet and Koumoutsakos [6]).

The DVH method exploits the operator splitting algorithm introduced by Chorin [2]. The single time step is divided in two sub-steps: one advective and one diffusive. In the advective sub-step, the velocity field is evaluated through a fast multipole method (FMM, see e.g. Graziani and Landrini [8]) while, in the diffusive sub-step, the diffusion of the vortices is performed using the deterministic algorithm described by Benson *et al.* [1]; the latter being based on a superposition of elementary solutions of the heat equation. If a body surface exists within the fluid domain, the no slip boundary condition is enforced through the generation of a vortex sheet, as described in Chorin [2].

In the diffusive step each vortex particle spreads its circulation on a Regular Point Distributions (RPD). At the end of this step, a new set of vortices is generated on the nodes of the RPD overwriting the previous one. This procedure avoids the excessive clustering or rarefaction of the vortices without using any remeshing (with interpolation procedure). To solve the diffusion near a smooth solid boundary, an homogeneous Neumann condition for the vorticity field is used, together with a flat plate approximation of the solid contour itself. However, the latter approximation is no more valid for the vortices close to geometrical singularities, no matter the level of the spatial discretization adopted.

In this work, the DVH method is used to simulate flows around bodies with non-smooth boundaries. The presence of geometrical singularities requires the modification of the diffusion algorithm described in Rossi *et al.* [20] with the introduction of a suitable visibility mask algorithm. This method is then tested around bodies of increasing complexities.

Exploiting the body-fitted approach, obtained through the RPD, is not a common approach. Indeed, a remeshing procedure is normally needed to correctly interpolate the vorticity field on a desired point distribution. For example in Wee and Ghoniem [23] a scheme treating diffusion and remeshing simultaneously is proposed and the appropriate interpolation Kernels are derived.

Moreover the use of the RPDs has the great advantage to be suitable for a body-fitted approach. Conversely a wide literature promotes the penalization function, which is an immersed-boundary like technique and it consists in a term that enforces continuity at the solid-fluid interface considering a simple rigid motion inside the solid. The method is deeply described in Mimeau *et al.* [12], where it was exploited to simulate the flow around a rotating blade and the flow past a semi-circular body with a porous layer, as well as in Rossinelli *et al.* [21], where an impulsively started cylinder at Re up to 1000 was simulated in order to evaluate the scalability of a vortex particle method on a GPU.

Because the high scalability aptitude of the particle codes, many other works analyse this topic: in Yokota and Barba [24] the performances of a tree-code and a Fast Multipole Method are compared on a GPU through the simulation of two leapfrogging vortex rings. In Yokota *e*t al. [25] the same Lagrangian approach was applied to the calculation of a decaying homogeneous isotropic turbulence and the results are compared with a spectral approach.

The paper is organized as follows: in section 2 the Diffused Vortex Hydrodynamics is outlined and a remark on the diffusion step is stressed in section 3 and deeply discussed in the presence of geometrical singularities in subsection 3.3. Some examples of the potentialities of the present numerical approach are offered in sections 4.1, 4.2, 4.3 and 4.4. In section 5 a discussion on the computation costs of the DVH method is reported. Finally conclusions close the article in section 6.

2 Diffused Vortex Hydrodynamics

A brief description of the DVH method is summarized in this section. A viscous incompressible fluid in the two-dimensional domain Ω is considered. The governing equations are the Navier-Stokes ones that, written in vorticity ω, reads as follows:

$$\frac{D\omega}{Dt} = \nu\nabla^2\omega, \qquad \forall \mathbf{r} \in \Omega\,. \tag{1}$$

where the time derivative is a material derivative, ν is the kinematic viscosity of the considered fluid and $\mathbf{r}$ is the position of a generic material point.

The vorticity field is discretized with N vortex particles in the following way:

$$\omega(\boldsymbol{r},t) = \sum_{i=1}^{N} \Gamma_i(t)\delta_\epsilon(\boldsymbol{r}-\boldsymbol{r}_i) \tag{2}$$

where Γ_i is the circulation of the i-vortex with position $\boldsymbol{r}_i$ and δ_ϵ is a smooth function that approximates the Dirac δ distribution in the weak sense.

In order to obtain a solution of eq. (1), the operator splitting scheme (Chorin [2],Chorin [3]) has been used. According to this method, the evolution of the fluid is split into two steps:

(i) the vortex particles are advected considering the fluid as inviscid,
(ii) the fluid is considered at rest and the vorticity is diffused due to viscosity.

During the advection step, the vorticity is transported according to the Euler equation:

$$\begin{cases} \dfrac{D\omega(\mathbf{r},t)}{Dt} = 0 \\ \dfrac{D\mathbf{r}}{Dt} = \mathbf{u}(\mathbf{r},t) \\ \nabla^2\mathbf{u}(\mathbf{r},t) = -\mathrm{curl}(\boldsymbol{\omega}),\ \boldsymbol{\omega} = \omega\mathbf{e}_3\,, \end{cases} \tag{3}$$

being $\mathbf{e}_3$ the unit vector orthogonal to the reference plane. In order to solve the Poisson equation for the velocity, the latter is decomposed in the following way:

$$\mathbf{u} = \mathbf{u}_\infty + \mathbf{u}_\omega + \mathbf{u}' \tag{4}$$

where $\mathbf{u}_\infty$ is the free stream velocity. The term $\mathbf{u}_\omega$ is the one induced by the vorticity distribution and can be evaluated by using the Biot-Savart law

$$\mathbf{u}_\omega(\mathbf{r},t) = \sum_{i=1}^{N} \Gamma_i\mathbf{K}_\epsilon(\mathbf{r}-\mathbf{r}_i) \tag{5}$$

through a classical Fast Multiple Method (FMM, see e.g. Graziani and Landrini [8]). In eq. (5) $\mathbf{K}_\epsilon$ is a regularization of the Biot-Savart kernel $\mathbf{K}$ (see e.g. Chorin [2]). The last term $\mathbf{u}'$ in equation (4) is a correction to the velocity caused by the presence of the boundary surfaces in the flow field. Computation of this term typically requires the use of boundary integral methods. An indirect Boundary Element Method (BEM) is here exploited through a discretization of the body surface with a set of sources with strength σ_j and point vortices with circulations γ_j:

$$\mathbf{u}'(\mathbf{r},t) = \sum_{j=1}^{N_b} [\gamma_j\mathbf{K}_\epsilon(\mathbf{r},\mathbf{r}_j) \,-\, \mathbf{e}_3 \times \mathbf{K}_\epsilon(\mathbf{r},\mathbf{r}_j)\sigma_j]\Delta s \tag{6}$$

for details see Rossi *et al.* [20]. The velocity $\mathbf{u}$ is then used to advect the vortex particles through a fourth order Runge-Kutta time integration scheme.

In step (ii) the vorticity diffusion is obtained by solving the following linear heat equation:

$$\frac{\partial \omega}{\partial t} = \nu \nabla^2 \omega \,. \tag{7}$$

In the DVH scheme this equation is solved by a deterministic diffusion algorithm proposed in Benson *et al.* [1] through a superposition of elementary solutions of the heat equation. More in details each vortex particle spreads the vorticity on a "Regular Point Distribution" (RPD) defined as a set of points with regular spacing without any topological connection. RPDs are generated using a packing algorithm described in Colagrossi *et al.* [4] and permits to arrange points around complex shapes distributing them with almost uniform spacing Δr. The algorithm provides a suitable distribution of points around complex bodies with a negligible CPU extra costs (for more detials see Rossi *et al.* [20]). The use of a packing algorithm avoids the pre-processing costs typical of FVM schemes for the mesh generation.

The vorticity field after diffusion is then lumped into new point vortices located at the RPD nodes. In fact, at the end of this step a new set of vortices is generated replacing the previous one. This procedure avoids the excessive clustering or rarefaction of the vortices. Further details can also be found in section 3.

In section 3 the solution of eq. (7) is addressed and discussed in a general case of solid boundaries.

2.1 Choice of diffusion and advection time steps

Considering U and L as the reference velocity and length of the problem, the Reynolds number is defined as $Re = UL/\nu$. For the sake of simplicity a single RPD is considered with the related spatial resolution equal to $L/\Delta r$. Following the derivation described in Rossi *et al.* [19], it is possible to associate the diffusive time step Δt_d to the spatial resolution $L/\Delta r$ and to the Reynolds number:

$$\Delta t_d \frac{U}{L} \simeq 0.34 \frac{\mathrm{Re}}{(L/\Delta r)^2} = 0.34 \frac{\mathrm{Re}_{\Delta r}}{(L/\Delta r)} \,, \tag{8}$$

being L the length scale of the specific problem at hand and $\mathrm{Re}_{\Delta r} = U\Delta r/\nu$ is the so-called Reynolds cell number. The latter needs to be $\mathcal{O}(1)$ at least in the region of interest in order to properly simulate all the vorticity spectrum.

Together with the diffusion time step, we need to consider also the time step, Δt_a, for the particles advection. This can be chosen by considering both the

flow velocity U and the discretization Δr. A first evaluation of Δt_a can be chosen as:

$$\Delta t_a \frac{U}{L} = \mathrm{Co} \frac{1}{(L/\Delta r)} \tag{9}$$

where the Courant number Co is $\mathcal{O}(10^{-1})$ to avoid that the vortex particles move with large displacements inducing extreme clustering or rarefaction on the particle distribution during the advection steps.

For the Reynolds number analysed in this work and for the ratios $L/\Delta r$ possible with the CPU resource available, the constrain on the advection step is generally more restrictive than that related to the diffusion process. This means that during a time interval Δt_d more than one advection step can be performed. This is true especially far from the boundary layer regions where coarser spatial discretizations and large $\mathrm{Re}_{\Delta r}$ are used. In order to synchronize diffusion and advection steps, Δt_a is arranged to get $\Delta t_d / \Delta t_a$ in an integer ratio:

$$N_{\Delta t} = \left[\frac{\Delta t_d}{\Delta t_a} \right] \rightarrow \Delta t_a = \frac{\Delta t_d}{N_{\Delta t}} \,. \tag{10}$$

3 Diffusion step with arbitrary solid boundaries

Using the boundary integral method it is possible to write a general solution of eq. (7) as (see *e.g.* Costabel [5]):

$$\begin{aligned} \omega(\mathbf{r},t) = -\nu \int_{t_0}^{t} \int_{\partial\Omega} \left[\mathcal{F}(\mathbf{r}^\star - \mathbf{r}, t-t') \frac{\partial \omega}{\partial n}(\mathbf{r}^\star) - \omega \frac{\partial \mathcal{F}}{\partial n}(\mathbf{r}^\star - \mathbf{r}, t-t') \right] d\mathbf{S}^\star dt' + \\ + \int_{\Omega} \omega(\mathbf{r}^\star, t_0) \mathcal{F}(\mathbf{r}^\star - \mathbf{r}, t-t_0) dV^\star, \end{aligned} \tag{11}$$

being $\partial\Omega$ the boundary of the fluid domain Ω while $\mathcal{F}(\mathbf{r}^\star - \mathbf{r}, t-t')$, the fundamental solution of the heat equation, is the Gaussian function:

$$\mathcal{F}(\mathbf{r}^\star - \mathbf{r}, t-t') = \frac{1}{4\pi\nu(t-t')} \exp\left\{ -\frac{|\mathbf{r}^\star - \mathbf{r}|^2}{4\nu(t-t')} \right\}, \tag{12}$$

$\omega(\mathbf{r}^\star, t_0)$ is the initial vorticity distribution, and n is the outward normal unit vector to $\partial\Omega$.

The natural evolution of the boundary integral formulation (11) to a solution procedure based on the approximation of the vorticity field by a finite number of point vortices is discussed in Graziani *et al.* [7].

Equation (11) takes a very simple form when dealing with free space problems

$$\omega(\mathbf{r},t) = \int_{\Omega} \omega(\mathbf{r}^\star,t_0)\mathcal{F}(\mathbf{r}^\star-\mathbf{r},t-t_0)dV^\star \tag{13}$$

where $\mathcal{F}(\mathbf{r}^\star-\mathbf{r},t-t_0)$ is the fundamental solution of the heat equation defined in eq. (12).

Calling $B_{\mathbf{r}'}$ the sphere $\{|\mathbf{r}'-\mathbf{r}| \leqslant R_d\}$ and following Rossi *et al.* [19], the approximated solution of the heat equation for a single point vortex with position $\mathbf{r}_i$ and strength Γ_i is given by:

$$\begin{cases} \omega(\mathbf{r},t_0+\Delta t_d) \;=\; \Gamma_i\,\mathcal{F}(\mathbf{r}_i-\mathbf{r},\Delta t_d) & \forall \mathbf{r}\in B_{\mathbf{r}_i} \\ \\ \omega(\mathbf{r},t_0+\Delta t_d) = 0 & \text{otherwise} \end{cases} \tag{14}$$

where the Gaussian distribution has been truncated at distance R_d for numerical purpose.

Eq. (14) can be used to distribute the vorticity of each vortex particle over its associated RPD which is characterized by a resolution length Δr. The vorticity field after the diffusion step is then lumped into new point vortices located at the RPD nodes.

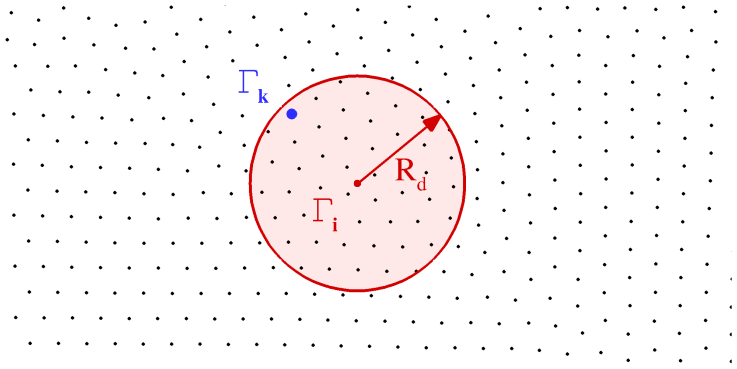

Fig. 1. Sketch of the vorticity diffusion of a vortex particles in free space with the associated RPD.

As sketched in Fig. 1, during the diffusive process the circulation of the i-th vortex particles gives a contribution Γ_k to the volume (area in 2D) ΔV_k associated to the k-th node of the RPD :

$$\Gamma_k = \Gamma_i\,\mathcal{F}(\mathbf{r}_i-\mathbf{r}_k,\Delta t_d)\,\Delta V_k\,. \tag{15}$$

In order to preserve the circulation Γ_i of the i-th donor particle on the different k-th acceptor nodes, a Shepard renormalization is implemented, evaluating a new circulation:

$$\Gamma'_k = \Gamma_i \frac{\Gamma_k}{\sum_k \Gamma_k} \tag{16}$$

where the summation $\sum_k \Gamma_k$ is extended to all the acceptor nodes inside the diffusive support $B_{\mathbf{r}_i}$ of the i-th particle. Eq. (16) will be used also in the case of diffusion near solid boundaries taking into account the image vortices introduced in the following.

3.2 Diffusion close to a solid boundary

After the advection step the non-slip boundary condition is violated and a vortex sheet is generated on the body wall according to the slip velocity obtained by eq. (4). In the following sub-step, in order to enforce the non-slip condition, the wall velocity is diffused within the field and eq. (11) can be used to evaluate this effect. In the diffusion step a vanishing normal derivative is assumed for the wall vorticity in eq. (11):

$$\left(\frac{\partial \omega}{\partial n}\right)_{\partial\Omega} = 0 \tag{17}$$

The second term in the boundary integral in eq. (11) disappears by choosing a function $\mathcal{F}_\Omega$ such that:

$$\left(\frac{\partial \mathcal{F}_\Omega}{\partial n}\right)_{\partial\Omega} = 0\,. \tag{18}$$

With this choice, eq. (11) reduces to

$$\omega(\mathbf{r}, t) = \int_\Omega \omega(\mathbf{r}^\star, t_0)\mathcal{F}_\Omega(\mathbf{r}^\star - \mathbf{r}, t - t_0)d\mathbf{r}^\star \tag{19}$$

where $\mathcal{F}_\Omega$ can be easily evaluated when $\partial\Omega$ is an infinite flat plate through the use of the image method. The presence of the boundary needs to be taken into account in the solution of eq. (11) if the vortex particle is at a distance lower than R_d.

The approximated solution for a single point vortex of position $\mathbf{r}_i$ and circulation Γ_i can then be written as (see Rossi *et al.* [20])

$$\omega(\mathbf{r}, t_0 + \Delta t_d) = \Gamma_i \left[\mathcal{F}(\mathbf{r}_i - \mathbf{r}, \Delta t_d) + \mathcal{F}(\mathbf{r}_i^{(im)} - \mathbf{r}, \Delta t_d)\right] \tag{20}$$

where $\mathbf{r}_i^{(im)}$ is the position of the image vortex. The solution (20) is defined for the point inside the ball $B_{\mathbf{r}_i}$ intersected with the half-space delimited by the tangential plane on the body (considering the outgoing normals of the body

surface). The image vortex gives its contribution only on the point belonging to the set $B_{\mathbf{r}_i} \cap B_{\mathbf{r}_i^{(im)}}$. A sketch of the influence areas commented above is depicted in figure 2.

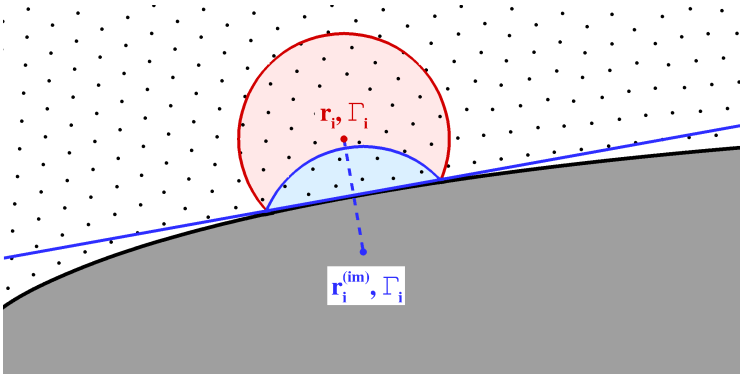

Fig. 2. Diffusion in the presence of a solid boundary: set of influence of the real and image vortex particles on the RPD nodes.

Equation (20) is strictly valid only for flat plate problems. However, when dealing with solid surfaces with generic shapes, if the diffusive radius R_d is small enough to make the body curvature not relevant, it is possible to locally approximate the body contour with a straight line. In this case it is possible to solve the diffusion near the body using the method just described.

Once the image vortex has been considered, both the image and the vortex give their diffusive contribution to the RPD nodes at a distance lower or equal to R_d along the body normal through (20).

To preserve the conservation of the circulation we must perform a renormalization procedure of the diffused vorticity using eq. (16) (for details see Rossi *et al.* [19]).

3.3 Diffusion in the presence of geometrical singularities

If the body presents geometrical singularities, the flat wall approximation described in the previous section is no longer valid and a visibility mask need to be properly defined. Differences arise depending on the distance of the vortex particle from the body as well as on the convexity or concavity of the area close to the singular points.

Elementary diffusion in region close to a sharp edge

To take into account the presence of an edge during the diffusive step, equation (20) must be modified. In particular the elementary solution for a single vortex

is approximated using a visibility mask to properly chose the RPD nodes over which the vorticity is diffused.

The action of the visibility mask is depicted in the left plot of Fig. 3: a vortex near an edge of the body is allowed to diffuse only in the area within a distance less or equal to R_d with the exception of the region shaded by the body. The definition of the shaded region is depicted in fig. 3 using the line passing from the vortex to the edge. Being $\mathbf{r}_i$ the position of a vortex, having circulation Γ_i, then the set of RPD points selected by the visibility mask can be called $B^{(vis)}_{\mathbf{r}_i}$.

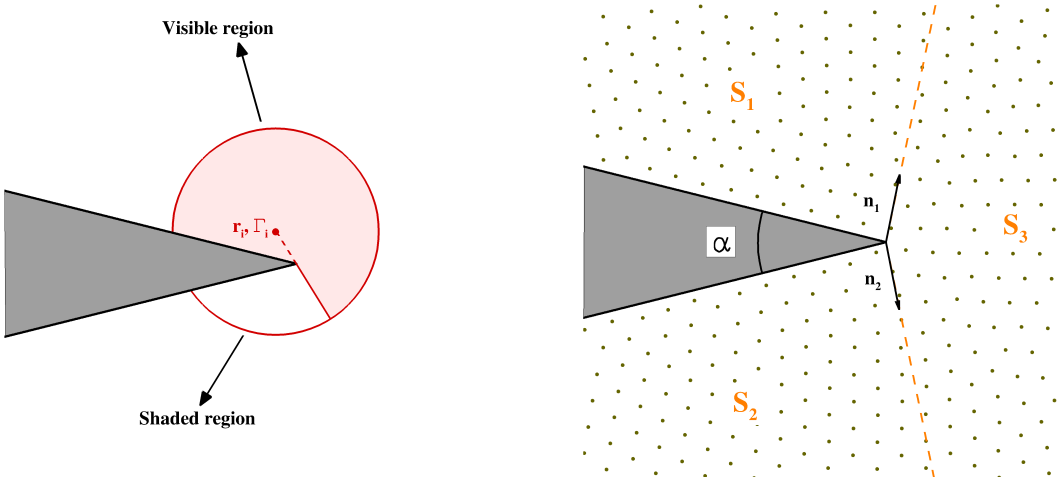

Fig. 3. Left: Action of the visibility mask algorithm. Right: Near body zone subdivision: $\mathbf{n}_1$ and $\mathbf{n}_2$ are the normal vectors on the two sides of the edge.

The effect of the body is then accounted for by defining an image vortex of position $\mathbf{r}_i^{(im)}$ and circulation Γ_i. The diffusion is then performed using equation (20) where the support $B_{\mathbf{r}_i}$ has been substituted by $B^{(vis)}_{\mathbf{r}_i}$. The position of the image vortex depends on the relative position of the vortex with respect to the edge of the body. Indeed, near an edge of the body three different zones S_1, S_2 and S_3 can be defined using the normal vectors $\mathbf{n}_1$ and $\mathbf{n}_2$ on the two side of the edge as depicted in the right plot of figure 3.

Fig. 4 sketches the four different possibilities for the definition of the visibility support and the position of the image vortex. The diffusive supports of the i-th vortex and of its image are $B^{vis}_{\mathbf{r}_i}$ and $B^{vis}_{\mathbf{r}_i^{(im)}}$ respectively. Vorticity is diffused by the i-th vortex particle inside $B^{vis}_{\mathbf{r}_i}$ while its image diffuses ω only over $B^{vis}_{\mathbf{r}_i} \cap B^{vis}_{\mathbf{r}_i^{(im)}}$.

In particular sketch 4(a) depicts the case of a vortex in zone S_1 at a distance larger than R_d from the edge, in this case the position of the image vortex is constructed as in section 3.2. Sketch 4(b) depicts the case of a vortex belonging to the zone S_1 at a distance smaller than R_d from the edge: also in this case the position of the image is constructed by reflection of the vortex position

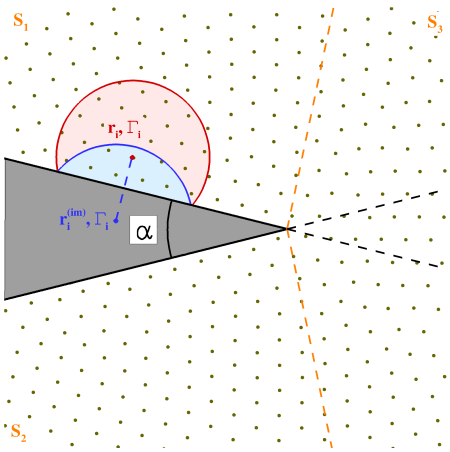

(a) Vortex in zone S_1 at a distance larger than R_d from the edge image position taken as the reflection with respect to the body tangent

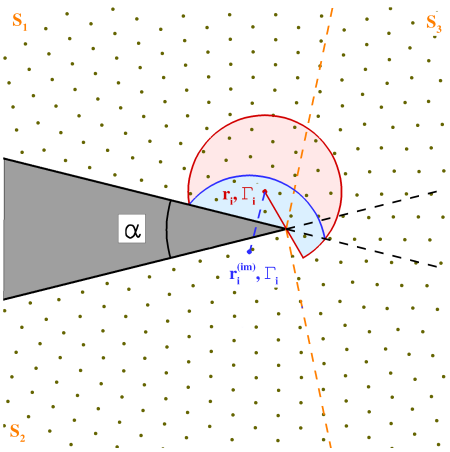

(b) Vortex in zone S_1 at a distance smaller than R_d from the edge image position taken as the reflection with respect to the body tangent

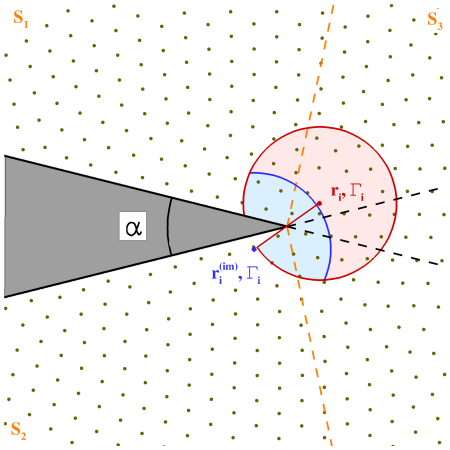

(c) Vortex in zone S_3 at a distance smaller than R_d from the edge image position taken as the reflection with respect to the edge position

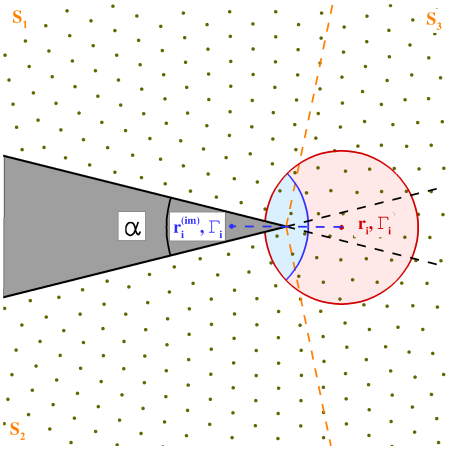

(d) Vortex in zone S_3 at a distance smaller than R_d from the edge image position taken as the reflection with respect to the edge position

Fig. 4. Image vortex position and diffusive influence zones. The red zones are the points on which only the vortex gives diffusive contribution. The blue zones are the points on which both the vortex and its image give diffusive contribution

with respect to the body tangent. Finally, in the sketches 4(c) and 4(d) the two cases of a vortex belonging to the zone S_3 are shown. In this case the image position is constructed by reflecting the vortex position with respect to the edge position.

The heat equation solution proposed above may appear quite crude for a single vortex particle, since it is based on a visibility criteria more suitable for an

hyperbolic problem than for a parabolic one. However, it must be stressed that the procedure is repeated and averaged for all the vortex particles in the neighbourhood of the edge making the errors of the above approximation negligible with respect to the overall accuracy of the method. Moreover the proposed algorithm guarantees the continuity of the solution in passing across the three regions S_1, S_2 and S_3.

It is worth to note that, similarly to other numerical approaches, if a geometry presents curvature radius smaller than the diffusive radius R_d this one cannot be resolved and need to be treated as a singular point.

Elementary diffusion in Concave region

Here a portion of the body surface characterized by a concave area defined by a sector of an angle α is considered. Fig. 5 depicts such an area with the associated RPD. Considering the generic i-th particle vortex with a diffusive radius R_d, it is possible to define three different zones S_1, S_2 and S_3 by using the following distance from the inner vertex:

$$\zeta = \frac{R_d}{\sin(\alpha/2)} \tag{21}$$

If the point vortex is in zone $S_3 = \{\zeta > \frac{R_d}{\sin(\alpha/2)}\}$ the diffusion is performed following the processes described in sections 3.2 and 3.3, because here the vorticity diffusion of the vortex particle is influenced by the closest wall only.

If the point vortex is inside zone $S_2 = \{\frac{R_d}{2\sin(\alpha/2)} \leq \zeta < \frac{R_d}{\sin(\alpha/2)}\}$ the diffusion

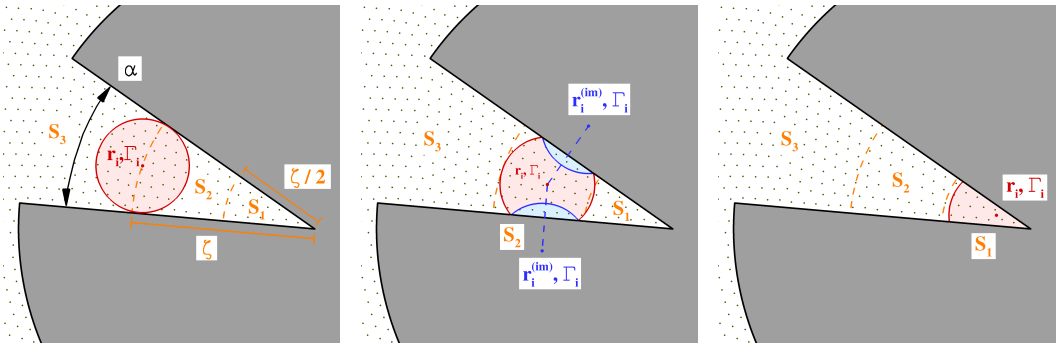

Fig. 5. Definition of three different areas for the diffusion process inside a concave region

is performed using the following equation:

$$\begin{cases} \omega(\mathbf{r}, t_0 + \Delta t_d) = \quad \Gamma_i \dfrac{1}{4\pi\,\nu\Delta t_d} \left[\exp\left\{ -\dfrac{|\mathbf{r}_i - \mathbf{r}|^2}{4\,\nu\Delta t_d} \right\} + \right. \\ \qquad\qquad \left. + \exp\left\{ -\dfrac{|\mathbf{r}_i^{(im)} - \mathbf{r}|^2}{4\,\nu\Delta t_d} \right\} + \exp\left\{ -\dfrac{|\mathbf{r'}_i^{(im)} - \mathbf{r}|^2}{4\,\nu\Delta t_d} \right\} \right] \forall \mathbf{r} \in B_{\mathbf{r}_i} \\ \omega(\mathbf{r}, t_0 + \Delta t_d) = 0 \text{ otherwise} \end{cases} \tag{22}$$

thus the circulation is diffused using two image vortices, one for each side of the body walls, to properly take into account their effect on the diffusion process. In this case the positions of the image vortices are constructed as explained in section 3.2 (see center plot of Fig. 5).

Going from S2 to $S_1 = \{\zeta \leq \frac{R_d}{2\sin(\alpha/2)}\}$ regions, the spanning of the areas influenced by the imaginary vortices increases until they become overlapped. In that configuration the spatial resolution does not allow to resolve gradients close to the wall, standing the dimension of the diffusive radius. For this reason, a simple renormalization procedure was chosen in order to simplify the algorithm, through the definition of the region S1.

4 Numerical test-cases

In this section some examples, highlighting the capabilities of DVH approach in the presence of geometrical singularities, are proposed.

Apart from the problem treated in section 4.4, for all the test-cases proposed the DVH results are compared with a Finite Volume Method (FVM), by means of an in-house solver (for details see *e.g.* [14], [15], [16], [17]), in order to discuss in details the quality of the DVH solutions. The comparisons are made on global quantities, drag and lift coefficients and also on local pressure distributions. This local analysis allows to check the effects on the flow solutions induced by the visibility mask algorithm.

In the DVH solver the flow is started impulsively, while the use of a ramp is more suitable in the FVM to avoid the inception of instabilities in the cells close to the body, where the no slip boundary conditions are imposed. Indeed, the cell volumes are highly packed along the normal direction of the body surface (because of high gradients involved) and the local time step needed to respect the stability constraints may become very small. For the above reason,

the detailed comparison between the two solvers is performed only when the steady or periodic regimes are reached.

Finally, in subsection 4.3 a non standard problem is considered, where a concave singularity is involved, is considered and the comparison with a Finite Volume code enlights the differences between a standard approach and the present one in treating such a singularity.

4.1 Flow past square and rectangular cylinder

A series of DVH simulations of the flow around square and rectangular cylinders with various angles of attack is here discussed.

In this section the Reynolds number and the lift and drag coefficients are made non dimensional using the maximum cross-stream length of the body d

$$Re = \frac{Ud}{\nu},\ c_d = \frac{2F_x}{\rho U^2 d},\ c_l = \frac{2F_y}{\rho U^2 d}.$$

Figure 6 depicts the definition of the maximum cross-stream height of the body d together with the angle of attack α and the sides A and B$\geq$A of the rectangle. The main parameters of the adopted space/time resolution are reported in Table 1. For all the simulations discussed in this section, the Reynolds number has been set equal to $Re = 200$ and the same spatial resolution has been used.

The first two simulations concern the flow around a square cylinder (A=B) with angles of attack $\alpha = 0°$ and $\alpha = 45°$. Figure 7 depicts the wake shed by the body for the two angles of attack used. We underline that for both the cases $\alpha = 0°$ and $\alpha = 45°$ the length d is fixed and the Reynolds number is

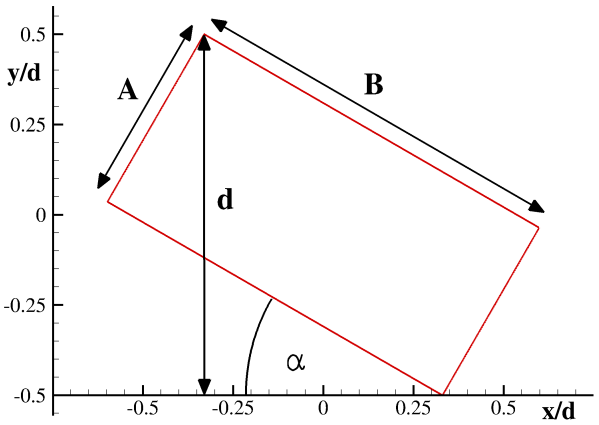

Fig. 6. Geometrical parameters for a flow simulation around a rectangular cylinder

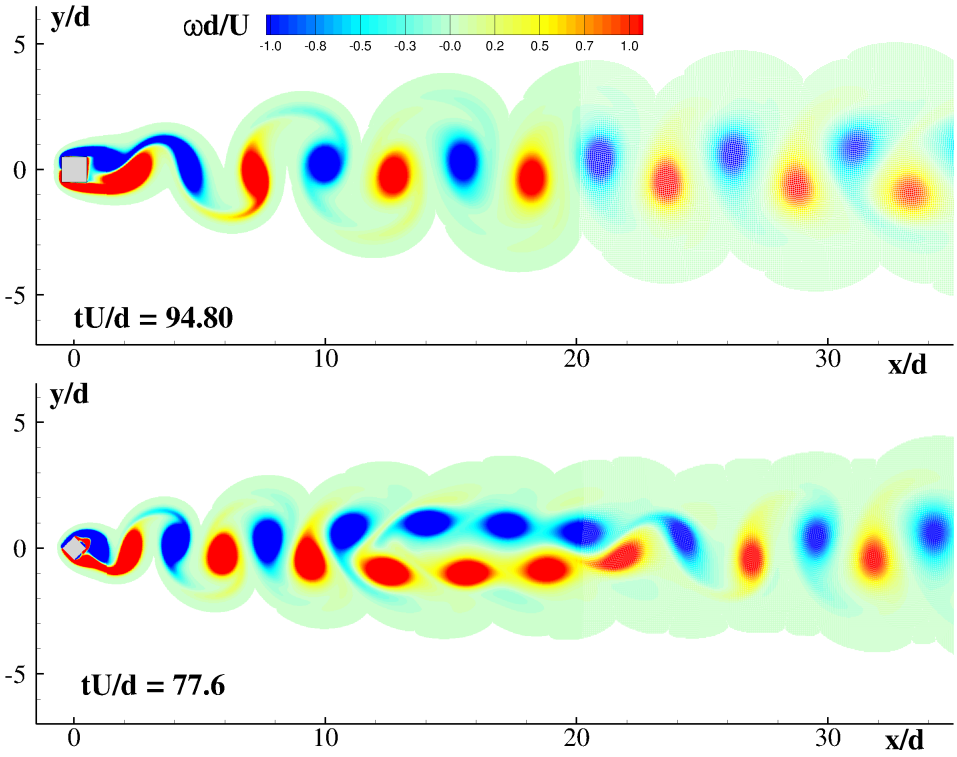

Fig. 7. Vorticity field for $d/\Delta r = 100$ for a square cylinder at $Re = 200$ and various angles of attack α. From top to bottom $\alpha = 0°$, and $\alpha = 45°$.

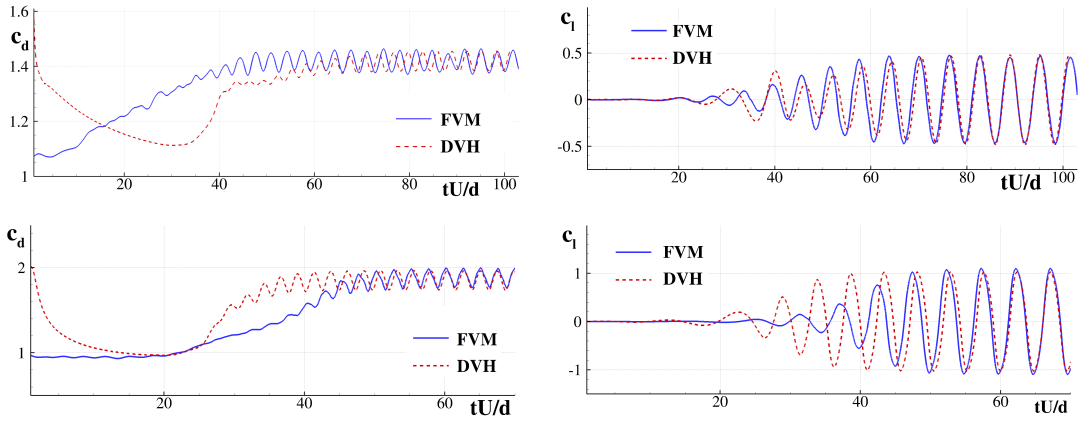

Fig. 8. Drag (left plot) and lift (right plot) coefficients for a flow past a square cylinder at $Re = 200$ and angle of attack $\alpha = 0°$ (top) and $\alpha = 45°$ (bottom). Comparison with a FVM solver is shown

$d/\Delta r$	$\mathrm{Re}_{\Delta r}$	Co	$\Delta t_a\, U/d$	$\Delta t_d/\Delta t_a$
100	2.00	0.70	7.05×10^{-3}	1

Table 1
Flow past a square and rectangular cylinders at Re = 200: main discretization parameters

set using this length, therefore the square with $\alpha = 0°$ is greater in size than the one adopted with $\alpha = 45°$.

The same analysis has been performed with the FVM solver in order to evaluate the loads. A comparison of the lift and drag coefficients is depicted in Figure 8 for $\alpha = 0°$ and $\alpha = 45°$ respectively with an evident fair agreement in the periodic regimes.

In order to evaluate the effect on the flow field of the edge ratio, the flow around a rectangular cylinder with $B = 2A$ and angles of attack $\alpha = 0°$ and $90°$ is investigated. Figure 9 depicts the wake shed by the body for $\alpha = 90°$. As is clearly visible in the figure, a complex interaction of the shed vortices appears after $x/d \sim 13$. A comparison of the lift and drag coefficients with

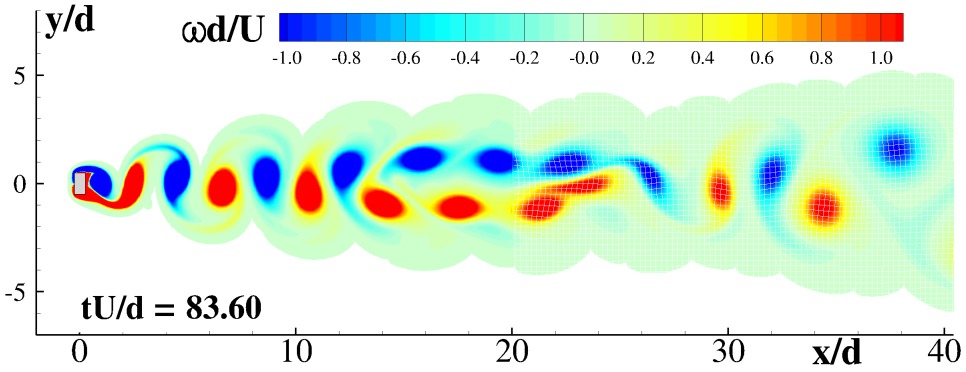

Fig. 9. Evolution of the vorticity field for $d/\Delta r = 100$ for a flow past a rectangular cylinder with $B/A = 2.0$ and angle of attack $\alpha = 90°$ at $Re = 200$.

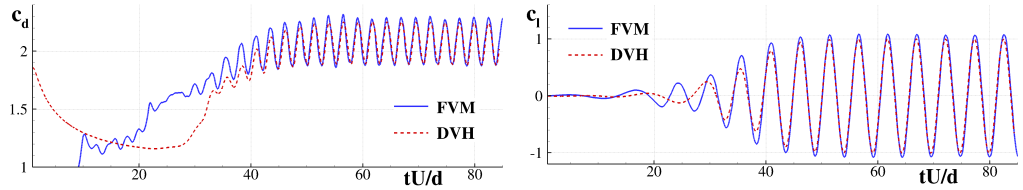

Fig. 10. Drag and lift coefficient for the flow past a rectangular cylinder with $B/A = 2.0$ at $Re = 200$ and $\alpha = 90°$. Comparison with a FVM solver is shown

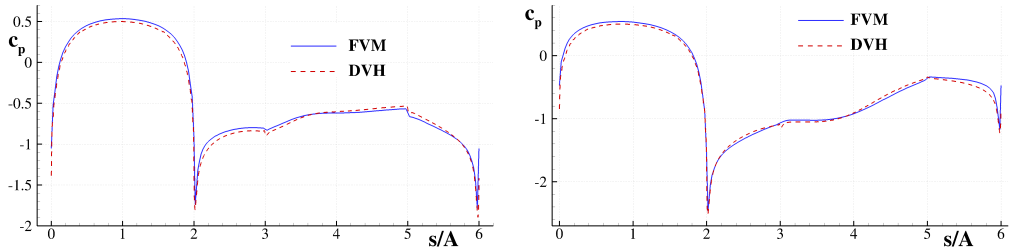

Fig. 11. Boundary distribution of pressure coefficient for the flow past a rectangular cylinder with $B/A = 2.0$ at $Re = 200$ and $\alpha = 90°$. Left: c_p taken at zero value of c_l. Right: c_p taken at maximum value of c_l. Comparison with a FVM solver is shown.

the results given by the FVM solver is depicted in Figure 10 and a good matching is obtained in the periodic regime. For this case, a comparison of the pressure coefficient along the body contour is also explored. The pressure distributions are evaluated, for this case and the following ones, during the periodic regime when the lift force is zero or at its maximum value. Figure 11 depicts the distribution of the pressure coefficient c_p comparing the DVH and FVM results. This comparison proves that the present method is consistent with a well tested finite volume procedure not only from a global point of view but also in the sense of the local quantities behaviour. In particular in the region close to the vertices, the pressure drops estimated by the two solvers are in a satisfactory agreement, demonstrating that the visibility mask procedure

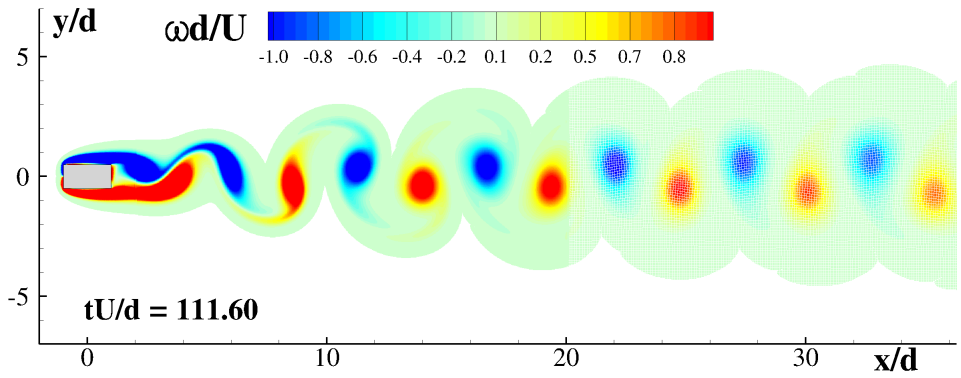

Fig. 12. Evolution of the vorticity field for $d/\Delta r = 100$ for the flow past a rectangular cylinder with $B/A = 2.0$ and angle of attack $\alpha = 0°$ at $Re = 200$.

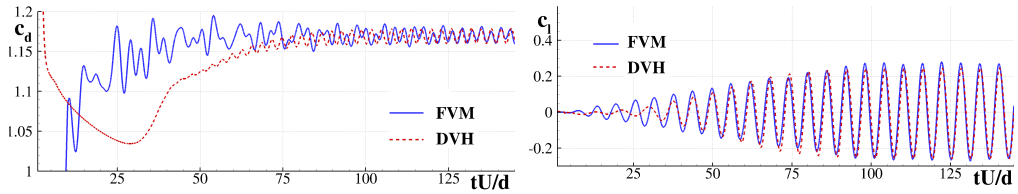

Fig. 13. Drag and lift coefficient for the flow past a rectangular cylinder with $B/A = 2.0$ at $Re = 200$ and $\alpha = 0°$. Comparison with a FVM solver is shown.

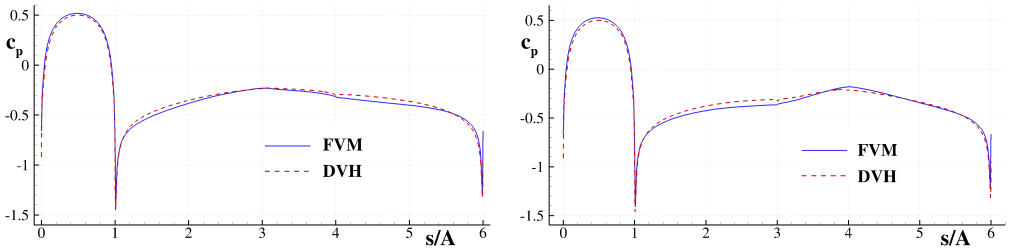

Fig. 14. Boundary distribution of the pressure coefficient for the flow past a rectangular cylinder with $B/A = 2.0$ at $Re = 200$ and $\alpha = 0°$. Left: c_p taken at zero value of c_l. Right: c_p taken at maximum value of c_l. Comparison with a FVM solver is shown.

reproduces in a correct physical way the local details of the numerical solution.

Figure 12 sketches the wake shed by the rectangle for $\alpha = 0°$: an evident difference with respect to the case $\alpha = 90°$ concerns the regularity of the vorticity fields in the two cases. In terms of global quantities, a comparison of the lift and drag coefficient with the FVM results has been performed and the results are compared in figure 13 with a good agreement in the periodic regime for both drag and lift components.

For this configuration with $\alpha = 0°$, a comparison of the pressure coefficient along the body contour with the FVM is again analysed and plotted in figure 14. The pressure distribution is nearly the same, with a perfect catch of the peak at the upstream corners.

4.2 Flow past an airfoil NACA0008

In the present section the flow around an airfoil NACA0008 with angle of attack $\alpha = 4°$ is discussed. Two different Reynolds numbers (based on the chord length c, $\mathrm{Re} = Uc/\nu$) 2000 and 6000 are simulated. Because of the small angle of attack and of the viscous regimes selected, the flow remains practically attached to the airfoil and the forces reach a steady regime after a start-up stage.

As stated in Mittal *et al.* [13]:

(i) these configurations have particular relevance for micro-aerial vehicles where Reynolds numbers tend to be in the range from 10^2 to 10^4,
(ii) this flow is quite challenging for numerical methods based on immersed boundary approaches since the region around the leading-edge of the airfoil has very small radius of curvature compared to the airfoil chord.

Therefore, a non-uniform mesh around this area is needed in order to resolve with a sufficient accuracy the boundary layer. In particular in both DVH and FVM the same mesh points across the boundary layer are used. In table 2 the main parameters of the space/time resolutions adopted in the DVH method are reported.

Re	$c/\Delta r$	$\mathrm{Re}_{\Delta r}$	Co	$\Delta t_a\, U/c$	$\Delta t_d/\Delta t_a$
2000	800	2.50	0.88	1.10×10^{-3}	1
6000	1000	6.00	2.11	2.11×10^{-3}	1

Table 2
Flow around an airfoil NACA0008 with angle of attack $\alpha = 4°$: main discretization parameters.

$c/\Delta r$	100	200	400	800
c_d	0.0866	0.0783	0.0769	0.0773
c_l	0.217	0.251	0.261	0.260

Table 3
Steady c_d and c_l for the NACA0008 with angle of attack $\alpha = 4°$, $Re = 2000$ and for different spatial resolutions $c/\Delta r$.

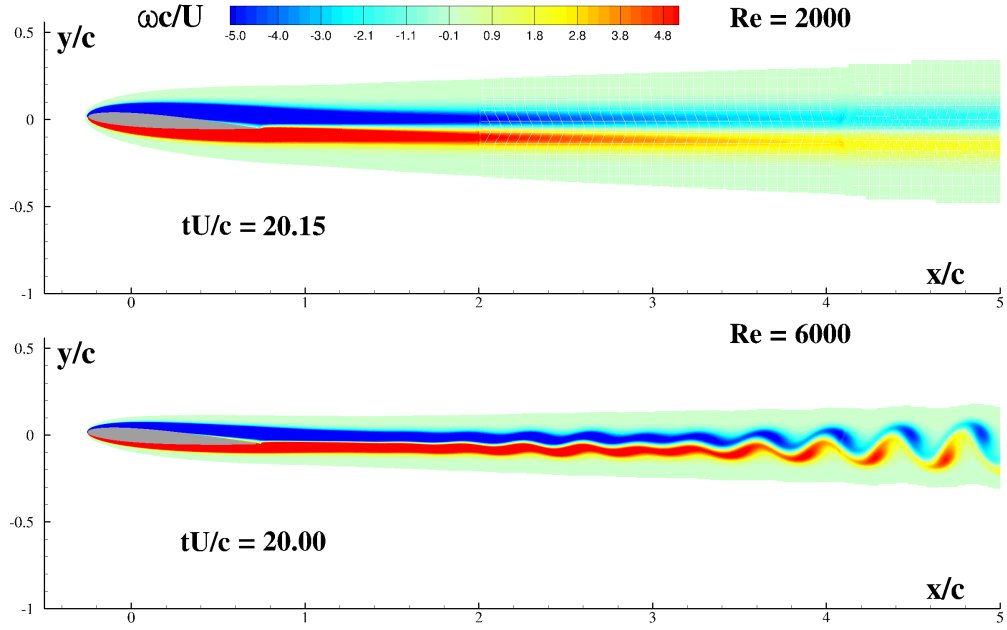

Fig. 15. Vorticity field for an airfoil NACA0008 with angle of attack $\alpha = 4°$ at two different Reynolds numbers.

This choice for the DVH quantities has been derived after convergence tests performed on the loads in the steady regime. Table 3 reports the steady drag and lift coefficients for different spatial resolutions at Re=2000. The convergence of the results is reached only for the last two spatial resolutions.

Figure 15 depicts the vorticity field for both the Reynolds numbers. In the simulation with $Re = 2000$ the wake is stable with the two shear layers remaining almost parallel. Conversely, at $Re = 6000$ at a distance of about two chords from the trailing edge, the wake becomes unstable giving birth to an oscillatory vortex street. However, this instability is too far from the airfoil to be detectable on the loads.

Figure 16 depicts an enlarged view of the vorticity field around the trailing edge for the two Reynolds studied. At Re=2000 the flow is practically attached to the airfoil and the separation is not clearly evident. Conversely, at Re=6000 the simulation shows that the flow separates from the suction side of the airfoil (see right plot of fig. 16). These results are in accordance with the one

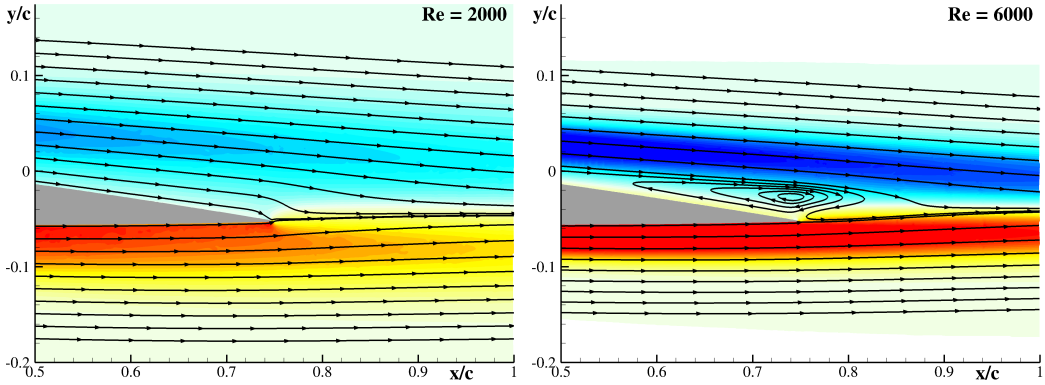

Fig. 16. Vorticity field and streamlines around the trailing edge of an airfoil NACA0008 with angle of attack $\alpha = 4°$ at Reynolds numbers 2000 (left) and 6000 (right) .

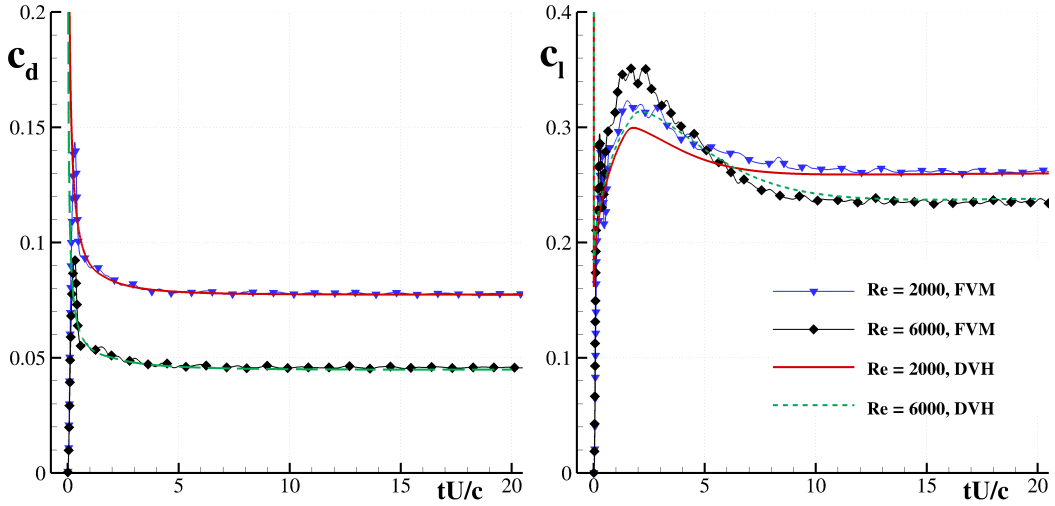

Fig. 17. Drag and lift coefficients for a flow past a NACA0008 airfoil with angle of attack $\alpha = 4°$ and two different Reynolds numbers. Data from FVM solver are also shown.

obtained by Kunz and Kroo [10] using a mesh based Navier-Stokes solver in a 2D framework.

Figure 17 depicts the time histories of the lift and drag coefficients for the two Reynolds numbers studied, comparing the DVH results with the data from the FVM solver. Once the steady regime is reached, the comparisons between the two solvers appear to be excellent for both the force components and for both the two Reynolds number.

Besides this comparison on global quantities, in order to better view the possible effects induced by the visibility mask procedure around the trailing

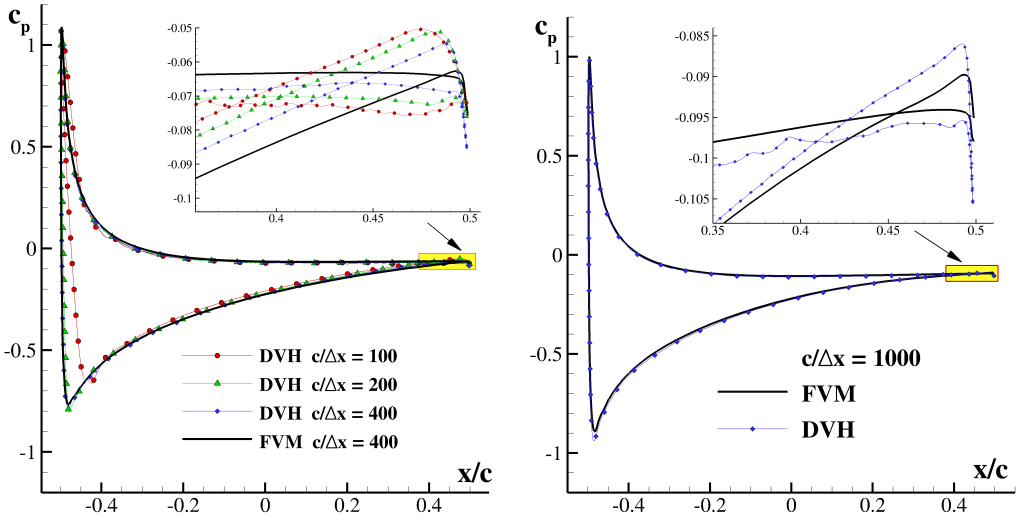

Fig. 18. Pressure coefficient for the flow around a NACA0008 profile with angle of attach $\alpha = 4°$ at $Re = 2000$ (left) and at Re = 6000 (right). Comparison with a FVM solver is shown.

edge, a comparison on the airfoil pressure distributions is performed and reported in figure 18. On the left plot of this figure, the c_p coming from the DVH at Re=2000 is shown for three different spatial resolutions. At $c/\Delta r = 400$ the convergence may be assumed reached. In the same figure an enlarged view around the trailing edge is reported. There the differences with the FVM converged solution are more visible, however the monothonic convergence of the DVH toward the FVM one remains well evident. This is a clear proof that the visibility mask procedure has only local effects on the numerical solution and that the related errors decrease when the spatial resolution is increased. On the right plot of figure 18 the pressure distribution at Re=6000 is reported for both solvers. The resolution adopted for both the codes is $c/\Delta r = 1000$ and the differences between the solutions is practically not detectable on a large scale. The comparison shown in the enlarged view of the same figure is aimed at stressing the local discrepancies around the trailing edge, confirming the satisfactory accuracy level of the proposed DVH scheme.

4.3 Flow past a circular cylinder without an angular sector

As third test case, the flow around a circular cylinder without an angular sector of 30° amplitude is here considered. The sector is positioned in such a way to avoid a symmetrical configuration, as sketched in Fig. 19.

A first comparison with the FVM solver is performed for Re = 100 and is aimed at demonstrating the capability of the DVH approach in treating concave geometries with singularities without any particular shrewdness.

In mesh-based method, the treatment of such a geometry is not trivial. Left plot of figure 20 shows the mesh exploited with FVM, where an overlapping grid technique is needed to properly treat the present topology. If a structured mesh is adopted in the FVM, in order to avoid the degeneration of the grid volumes close to the singularity, a simplified geometry is assumed using a small circle enclosing the tip as sketched in the right plot of figure 20. In a 2D framework this kind of mesh adjustments are accessible while for 3D it may require great efforts.

Figure 21 depicts the time histories of the drag and lift coefficients at Re = 100. When the periodic regime is reached, a good agreement between DVH and FVM solvers is obtained. To better show the main features of the flow field and in order to highlight the complexity of the problem, the pressure and the vorticity fields are reported in figure 22 when the lift reaches its maximum value. The spatial resolution adopted for the DVH is $c/\Delta r = 200$. The FVM simulation is carried out with a space and time discretization coherent with

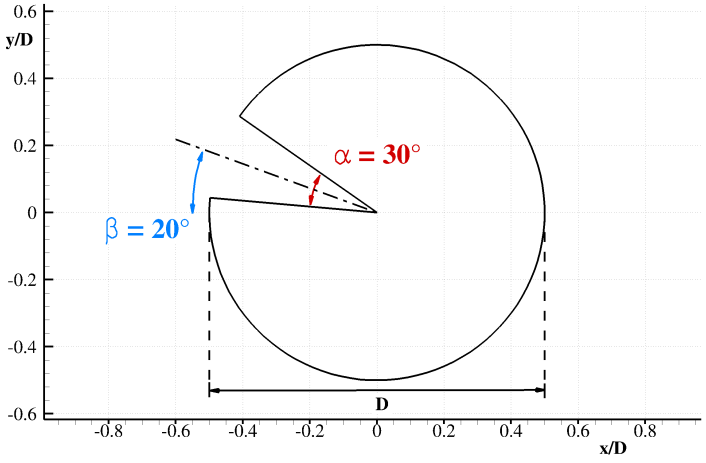

Fig. 19. Geometric configuration of a circular cylinder without an angular sector.

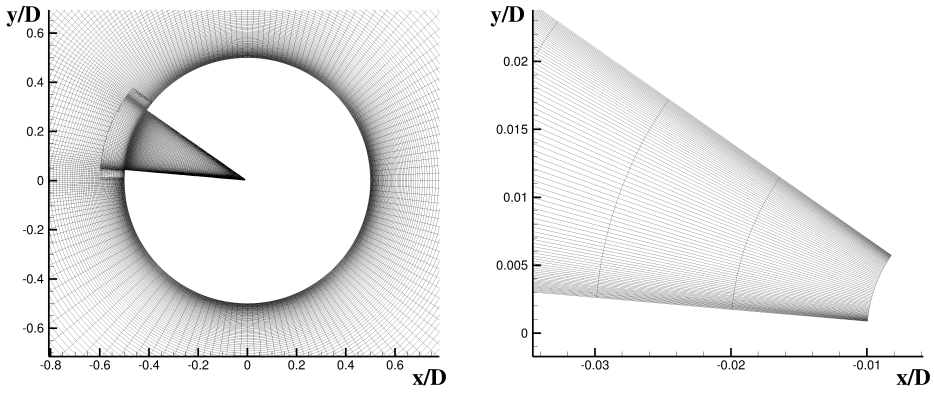

Fig. 20. Finite Volume numerical grid, exploiting an overlapping grid algorithm. Left: overall view. Right: tip magnification.

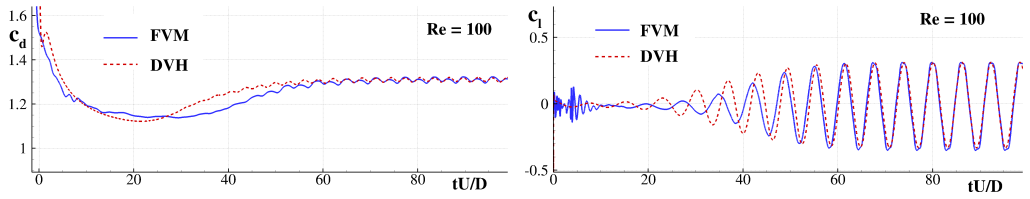

Fig. 21. Flow around a circular cylinder without an angular sector: Drag and lift coefficient at Re = 100. Comparison with a FVM solver is shown.

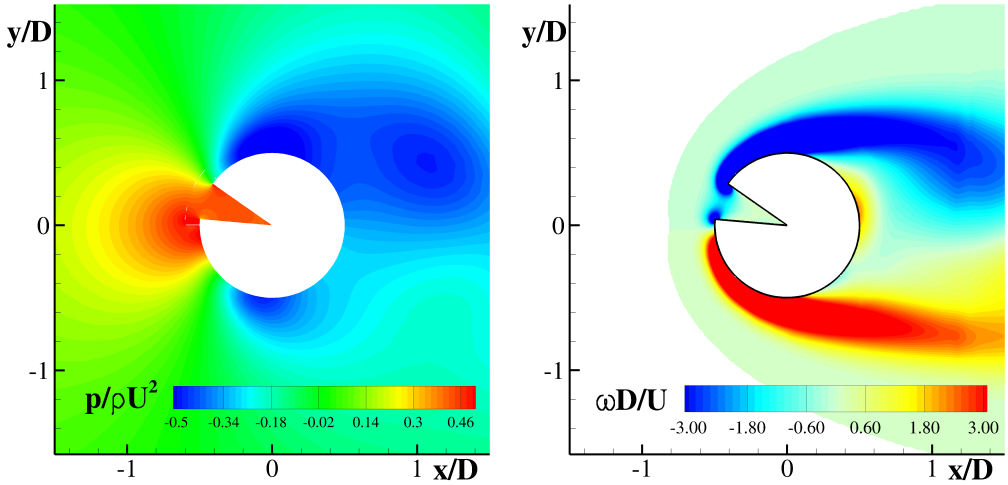

Fig. 22. Flow around a circular cylinder without an angular sector at Re = 100: pressure field (Left) and vorticity field (Right) at the maximum lift.

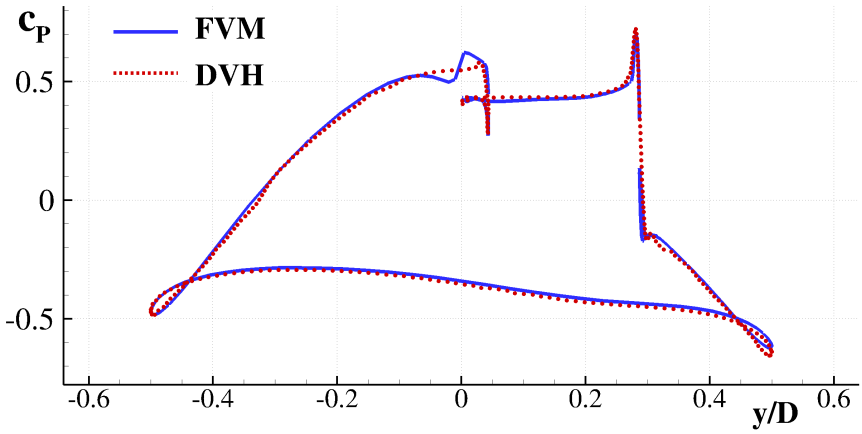

Fig. 23. Flow around a circular cylinder without an angular sector at Re = 100: pressure profile from DVH and FVM solvers calculated at the maximum lift.

the DVH ones in order to avoid under resolved solutions. In order to perform a local comparison of the two solutions, the pressure profiles along the solid body are depicted in figure 23. Also for this geometry, the two solvers show a good accordance but for small discrepancies. In particular, the pressure evaluated near the vertices are practically superimposed, demonstrating that

also the diffusion procedure adopted for the concave regions is suitable for getting good numerical results.

As a second test-case, the same geometry is used for studying the flow at Re $= 10,000$. This problem is more demanding because it involves quite complex vorticity patterns. To the purpose, the spatial resolution is increased to $D/\Delta r = 800$ in order to correctly reproduce the boundary layer regions.

In Fig. 24 the vorticity fields of the DVH and FVM solvers are compared during

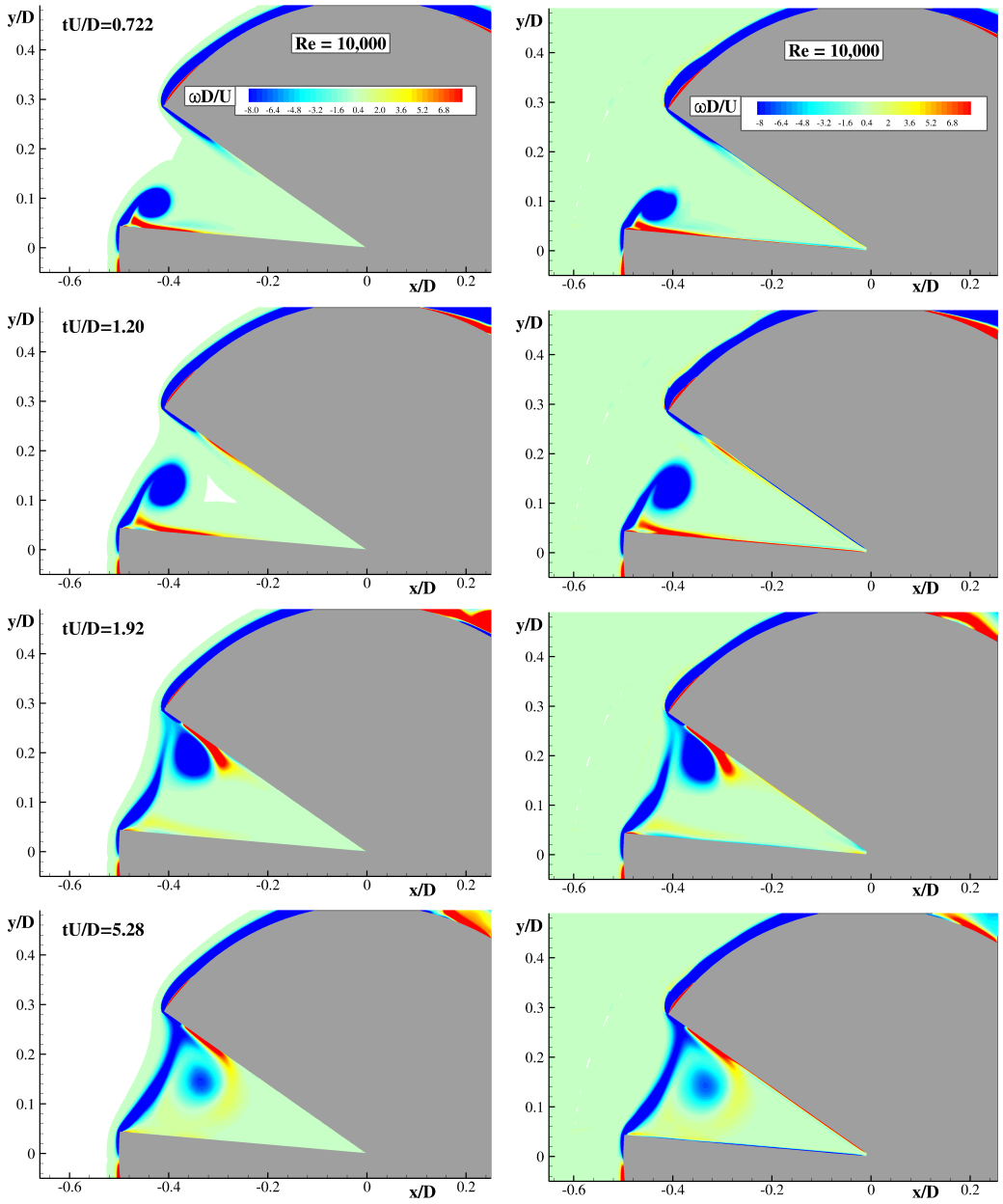

Fig. 24. Vorticity fields at several time instants, Re = 10,000. Left column: DVH. Right Column: Finite Volume Method.

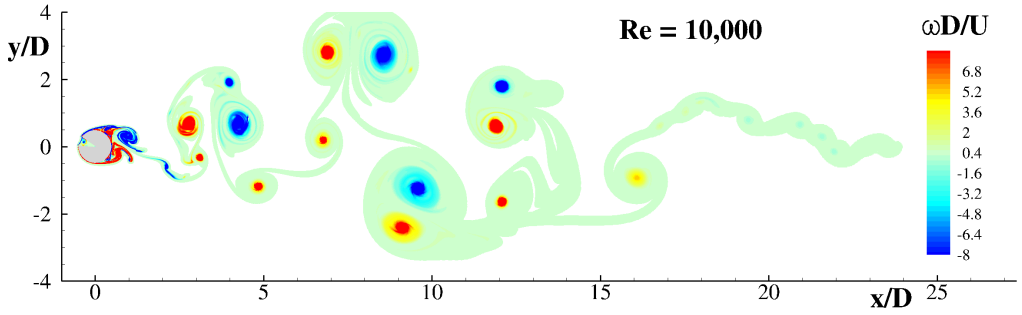

Fig. 25. Far wake of the cylinder without an angular sector at $Re = 10,000$, DVH.

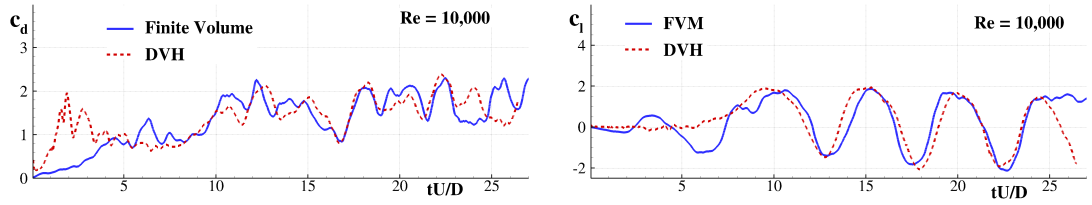

Fig. 26. Time hystories of drag (left) and lift (right) forces for DVH (line) and FVM (symbols) approaches.

the transient regime. At the initial stages a negative vorticity puff originates from the lower corner of the sector and travels towards the upper corner. When it impinges the edge above, it bends and rolls up and a driven cavity flows is established inside the concave region for a limited time because of its intrinsic instability. The comparison between DVH and FVM approaches is quite fair, even if spurious vorticity at the solid surface is present in the FVM because of the numerical derivation used on the FVM velocity field.

Concerning with a longer time evolution, in Fig. 25 the far wake of the body is plotted. It shows a vorticity pattern characterized by the presence of big scale dipolar structures emerging from the inverse cascade mechanism, typical of two-dimensional turbulence, and leading to a strong chaotic behaviour.

In fig. 26 the time histories of the forces calculated by DVH and FVM solver are shown. The mean values of drag and the amplitude of the lift force match in a satisfactory way. It is worth to underline that a pointwise comparison in time is not possible since a periodic regime does not exist at this Reynolds number. This implies that it is not possible to get a local convergence of the solution neither with the DVH nor with the FVM. Therefore, only a "statistical" approach can be suitable in order to detect a convergence, for example on the average load levels and on the related RMS. However, to perform this kind of measures very long time histories are needed.

4.4 Flow past a DDG-51 hull waterline

A simulation around a model ship of the USS Arleigh Burke (DDG-51) has been performed as a final test case. The ship model, having a length L_{pp} of 2.17 meters, is supposed to advance with a steady drift angle with a low speed of 4.61 cm/s corresponding to a Froude number, Fr, equal to 0.01 and to a Reynolds number Re=100,000. In this condition, being the Froude number very low, the free surface can be considered unperturbed (no waves are generated) as may happen for a ship manoeuvring in a harbour. In this case it is possible to study the generation of vorticity along the waterline of the ship and its consequent downstream advection.

The main discretization parameters of the simulation are given in table 4.

Re	Fr	$L_{pp}/\Delta r$	$\mathrm{Re}_{\Delta r}$	Co	$\Delta t_a\, U/L_{pp}$	$\Delta t_d/\Delta t_a$
100,000	0.01	3200	31.25	1.84	5.74×10^{-4}	1

Table 4
Flow around the waterline of a DDG-51 shiphull advancing with a steady drift angle: main discretization parameters.

At such high Reynolds number the vorticity field generated by a ship geometry becomes more complicated with respect to the previous cases. In particular the waterline in the bow region is characterized by a sharp edge with a change of the concavity sign at a distance from the bow edge of about 0.1 L_{pp}.

Figure 27 depicts six time instants of the evolution of the vorticity field highlighting the presence of a wide range of vortical scales in the starboard region. As expected by the drift condition a large recirculation area is formed and it is possible to note a zone close to the stern in which the detached vortices travels upstream, moving toward the bow of the ship along the hull side. Figure 27 depicts the evolution of an isolated vortex (highlighted by a black arrow). The latter is released in the bow region, convected toward the stern and finally it interacts with the boundary layer originating a dipole structure. After this, it travels towards the bow where it merges with the other vortices.

A further example of the complex shedding and evolution of the vorticity field is depicted in the last row of figure 27, where a series of small vortices are shed from the ship bow. These vortices interact with a bigger one starting to orbit around it creating a complex "flower shaped" vorticity structure. The shedding of such small vortices induces high frequency components on the local loads and may generate relevant vibration on the ship structure.

Finally, in figure 28 the far wake generated by the advancing ship is sketched.

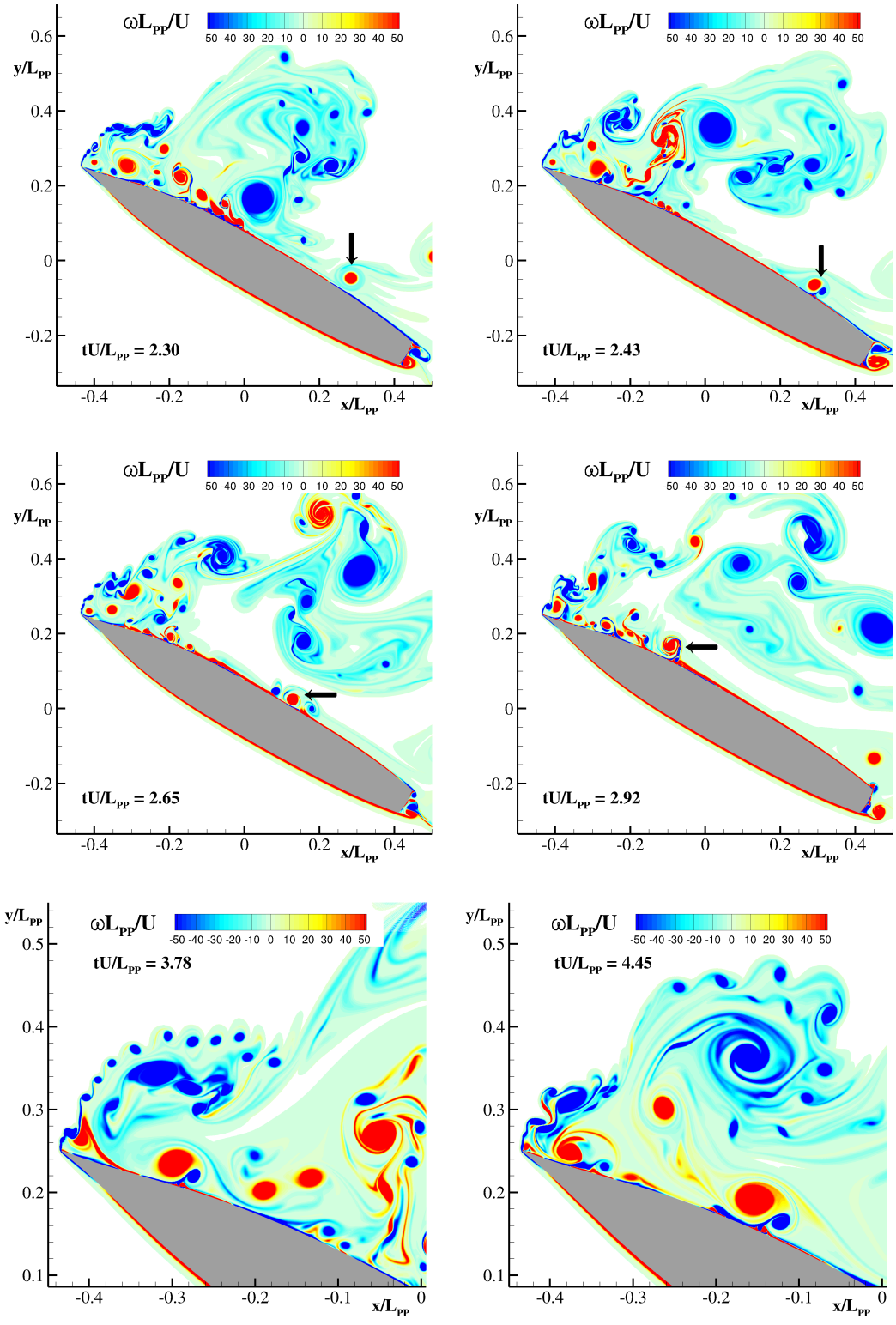

Fig. 27. Evolution of the vorticity field around the starboard region of the ship DDG-51 advancing with a Froude number Fr=0.01 with a drift angle of 30 degrees.

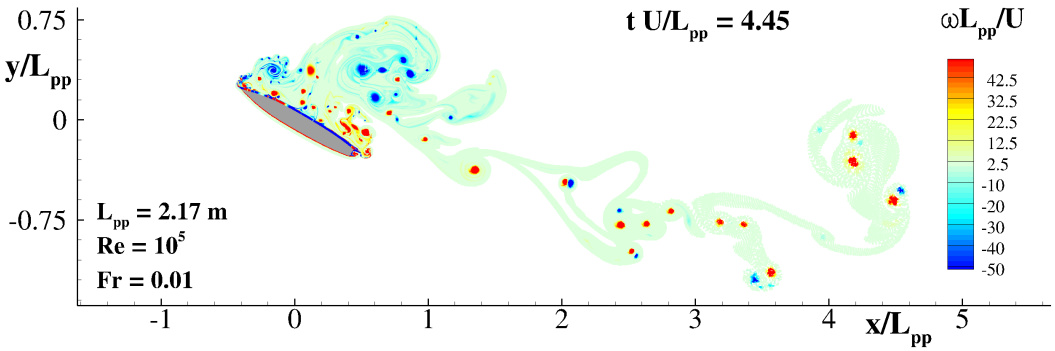

Fig. 28. Vorticity field generated by the waterline of a DDG-51 shiphull advancing with a steady drift angle $\alpha = 30°$ at a low Froude number Fr $= 0.01$

5 Computational resources

The test cases used in this work are labelled in table 5.

All the DVH simulations have been performed on a desktop PC with six cores Xeon(R) CPU X5650, 2.3GHz, using a simple OpenMP parallel programming. The CPU cost of the implemented code is about 100μs per vortex particle and per time iteration on a single core. This cost is inline with other vortex particle solvers and mainly linked to the Fast Multipole Method for the solution of the Poisson equation. The maximum number of used particle is of order 10^6 and the allocated memory did not exceed 1 Gbyte.

Table 6 displays, for some test-cases studied in this work, the total CPU cost and the main adopted parameters. The CPU cost of the test-case $N° 8$ justifies the limit in section 4.3 to get very long time behaviour for this kind of flow using desktop PCs. A confirmation of the CPU costs reported in this section is also stated in the recent article Rossinelli *et* al. [26] where a FMM technique with Adaptive Mesh Refinement (AMR) is used, the 2D flows around bodies at Re $> 1,000$ were studied in limited physical time ranges similarly to the ones adopted in this work.

The CPU costs of the FVM solver are comparable with the DVH ones when using the same time step and a number of grid cells similar to the number of vortices used in the DVH. However, the comparisons between the two solvers cannot be performed in a straightforward way, since different important aspects need to be taken into account. First of all for the FVM, pre-processing is more demanding since the meshes need to be prepared. Secondly, the DVH scheme has a self-adaptivity (i.e. vorticity formulation allows to discretize only the rotational region), while in the FVM the mesh must be designed in an optimum way with a-priori knowledge of the areas interested by high velocity gradients. For this reason recently AMR algorithms are often adopted, however, generally the computational costs (for each node and each iteration)

Test $N°$	Geometry	Re	Angle of attack
1	Square cylinder	200	0°
2	Square cylinder	200	90°
3	Rectangular cylinder	200	90°
4	Rectangular cylinder	200	0°
5	NACA0008 profile	2000	4°
6	NACA0008 profile	6000	4°
7	Circular cylinder without an angular sector	100	20°
8	Circular cylinder without an angular sector	10,000	20°
9	DDG-51 hull waterline	100,000	30°

Table 5
Then nine test-cases studied in the present work.

	Test $N°1$ Re=200	Test $N°6$ Re=6000	Test $N°8$ Re = 10,000	Test $N°9$ Re=100,000
$L/\Delta r$ close to the body	100	1000	800	3200
N_{Max} vortices	520,000	600,000	1,400,000	5,220,000
N° iterations	14,341	9,456	9,600	7,763
$t_{end}U/L$	100	20	26	4.45
$\Delta t_a\, U/L$	$7\,10^{-3}$	$2\,10^{-3}$	$2.7\,10^{-3}$	$5.7\,10^{-4}$
CPU time (6 cores)	30 hours	24 hours	3 days	8 days

Table 6
DVH solvers CPU time costs for simulating four of the test-cases proposed in this work. Here L is a characteristic length of the problem.

rise with respect to a classic FVM solver with a fixed mesh. Summarizing, the question related to which solver between DVH or FVM can be the more performing one and in which conditions, still remains an open issue.

It is interesting that recently some researchers are moving in the direction of coupling the two methodologies in order to get benefits from each model. For example in the recent work of Palha *e*t al. [27] the FVM is used close to the solid body while a Vortex Particle Method is adopted in the wake region. This idea of coupling the Vortex Particle Method with mesh-based method was initially developed in the past by Cottet [28] and by Ould-Salihi *e*t. al. [29].

6 Conclusions

In the present paper the capabilities of Diffused Vortex Hydrodynamics (DVH) approach in treating the vorticity dynamics around geometrical singularities have been explored. The definition of a visibility mask allowed to correctly diffuse the vorticity over the nodes of a Regular Point Distribution even in the presence of a sharp edge or of a concave region. In order to assess the potentialities of the meshless numerical scheme, some examples have been offered, starting by square/rectangular sections and NACA profiles for which reference data are obtained through a Finite Volume Method. The last two cases studied are particularly intriguing: the flow around a cylinder without a sector (see section 4.3) and the flow past a DDG-51 hull (see section 4.4). In the former, a concave region is involved and a comparison with a Finite Volume approach allowed to discuss the problems experienced by the latter in taking into account such a singularity.

An accurate discussion of the vorticity field generated over the free surface by a sharp bow hull advancing in steady drift is finally performed. The interaction of a vortices of different scales gives rise to very peculiar structures rarely discussed in the literature as far as to the authors knowledge.

Important steps forward will be achieved with the inclusion of the extension of the DVH model in three-dimensions framework.

Acknowledgements

The research leading to these results has received funding by the Flagship Project RITMARE - The Italian Research for the Sea - coordinated by the Italian National Research Council and funded by the Italian Ministry of Education, University and Research within the National Research Program 2015-2016.

References

[1] M.G. Benson, P.G. Bellamy-Knights, J.H. Gerrard, I. Gladwell, A viscous splitting algorithm applied to low reynolds number flows round a circular cylinder. *Journal of Fluids and Structures*, 3(5):439-479, 1989.

[2] A.J. Chorin, Numerical study of slightly viscous flow. *Journal of Fluid Mechanics*, 57:785-796, 1973.

[3] A.J. Chorin, Vortex sheet approximation of boundary layers. *Journal of Computational Physics*, 27(3):428-442, 1978

[4] A. Colagrossi, B. Bouscasse, M. Antuono, S. Marrone, Particle packing algorithm for SPH schemes. *Computer Physics Communications*, 183(2):1641-1683, 2012.

[5] M. Costabel, Boundary integral operators for the heat equation, *Integral Equations and Operator Theory*, 13(4): 498-552 , Birkhäuser-Verlag, 2001

[6] G.H. Cottet, P.D. Koumoutsakos, *Vortex Methods: Theory and Practice.* Cambridge University Press, University Printing House, Shaftesbury Road, Cambridge, United Kingdom, 2008.

[7] G. Graziani, M. Ranucci, R. Piva, *From a boundary integral formulation to a vortex method for viscous flows.* Computational mechanics 15.4 (1995): 301-314.

[8] G. Graziani, M. Landrini, Application of multipoles expansion technique to two-dimensional nonlinear free-surface flows. *Journal of ship research*, 43(1): 1-12, 1999.

[9] P. Koumoutsakos, A. Leonard, High-resolution simulations of the flow around an impulsively started cylinder using vortex methods. *Journal of Fluid Mechanics*, 296:1-38, 1995.

[10] P.J. Kunz, H. Kroo, Analysis and design of airfoils for use at ultra-low Reynolds numbers, *Progress in Astronautics and Aeronautics*, pp. 35-60 , American Institute of Aeronautics and Astronautics, 2001

[11] S. Marrone, M. Antuono, A. Colagrossi, G. Colicchio, D. Le Touz, G. Graziani, δ-SPH model for simulating violent impact ows *Computer Methods in Applied Mechanics and Engineering*, 200: 1526-1542, 2011.

[12] C. Mimeau, F. Gallizio, G.H. Cottet, I. Mortazavi, Vortex penalization method for bluff body flows *International Journal for Numerical Methods in Fluids*, 2015.

[13] R. Mittal, H. Dong, M. Bozkurttas, F.M. Najjar, A. Vargas, A. von Loebbecke, A versatile sharp interface immersed boundary method for incompressible flows with complex boundaries, *Journal of computational physics*, 227(10): 4825-4852, 2008

[14] A. Di Mascio, R. Broglia and B. Favini, A second order godunov-type scheme for naval hydrodynamics. *Godunov methods: theory and applications*, 253–261, Springer Science & Business Media, 2001

[15] R. Muscari, R. Broglia, A. Di Mascio, An overlapping grids approach for moving bodies problems. *The Sixteenth International Offshore and Polar Engineering Conference*, 28 May-2 June, San Francisco, California, 2006.

[16] A. Di Mascio, R. Broglia, R. Muscari, On the application of the single-phase level set method to naval hydrodynamic flows. *Computers & Fluids*, 36(5): 868–886, 2007

[17] A. Di Mascio, R. Broglia, R. Muscari, Prediction of hydrodynamic coefficients of ship hulls by high-order Godunov-type methods. *Journal of Marine Science and Technology*, 14(1): 19–29, 2009

[18] N. A. Petersson, Hole-Cutting for Three-Dimensional Overlapping Grids. *SIAM Journal on Scientific Computing*, 21(2): 646-665, 1999.

[19] E. Rossi, A. Colagrossi, G. Graziani, Numerical Simulation of 2D-

Vorticity Dynamics using Particle Methods. *Computers and Mathematics with Applications*, 69, pp. 1484-1503, 2015

[20] E. Rossi, A. Colagrossi, B. Bouscasse, G. Graziani, The Diffused Vortex Hydrodynamics method. *Communications in Computational Physics*, 18(2), pp. 351-379, 2015.

[21] D. Rossinelli, M. Bergdorf, G.H. Cottet, P. Koumoutsakos, GPU accelerated simulations of bluff body flows using vortex particle methods *Journal of Computational Physics*, 229(9), pp. 3316-3333, 2010.

[22] D. J. Y. Villareal, Vortex resonance wind turbine *US Patent App. 13/811,788*, Google Patents, 2013.

[23] D. Wee, A. F. Ghoniem, Modified interpolation kernels for treating diffusion and remeshing in vortex methods *Journal of Computational Physics*, 213(1), pp.239-263, 2006.

[24] R. Yokota, L. A. Barba, Comparing the treecode with FMM on GPUs for vortex particle simulations of a leapfrogging vortex ring *Computers & Fluids*, 45(1), pp. 155-161, 2011.

[25] R. Yokota, T. K. Sheel, S. Obi, Calculation of isotropic turbulence using a pure Lagrangian vortex method *Journal of Computational Physics*,226(2), pp. 1589-1606, 2007.

[26] D. Rossinelli, B. Hejazialhosseini, W. van Rees, M. Gazzola, M. Bergdorf, P. Koumoutsakos, MRAG-I2D: Multi-resolution adapted grids for remeshed vortex methods on multicore architectures *Journal of Computational Physics*, 288, pp. 1-18, 2015.

[27] A. Palha, L. Manickathan, C.S. Ferreira and G. van Bussel, A hybrid Eulerian-Lagrangian flow solver *arXiv preprint arXiv:1505.03368*

[28] G.H. Cottet, Particle-grid domain decomposition methods for the Navier-Stokes equations in exterior domains *Lectures in Appl. Math.*, 28, pp. 100-118, 1991.

[29] M. Ould-Salihi, G.H. Cottet and M. El Hamraoui, Blending finite-difference and vortex methods for incompressible flow computations *SIAM J. Sci. Comp.*, 22, pp. 1655-1674, 2000